Geophys. J. Int. (2004) **158,** 625–636 doi: 10.1111/j.1365-246X.2004.02306.x

A scattering region near the core–mantle boundary under the North Atlantic

Luisa Braña[1,2]* and George Helffrich[1]

[1]*Department of Earth Sciences, University of Bristol, Wills Memorial Building, Queens Road, Bristol* BS8 1RJ*, UK*
[2]*Earthquake, Forensic Seismology and Geomagnetism Programme, British Geological Survey, Murchison House, West Mains Road, Edinburgh EH9 3LA, UK.*

Accepted 2004 March 18. Received 2004 February 20; in original form 2001 November 13

SUMMARY

We analysed *PcP* precursors in seven events from Central America, recorded at the UK array of short-period stations, to determine the most likely source of this signal. Combinations of observations of slowness, traveltime and backazimuth were used to investigate the properties of the phase, with the result that its source is identified as *P* to *P* scattering from an anomalous region in the lower mantle, within D″. Using a joint likelihood method, the best estimate of a point source for scattering is at 44.0°N, 71.5°W (under Nova Scotia) and 2720 km depth. Analysis of the spectrum of the scattered signal indicates that the region contains small-scale heterogeneities on the order of 0.6 to 0.7 km, and is ∼700 km in size. The velocity contrast between the scattering bodies and ambient mantle is as high as +0.4 to +0.7 per cent *Vp* and +1.4 to +6.6 per cent *Vs*. On account of their small size, positive velocity anomaly and association with the reconstructed position of ancient subducted material, we conclude that they represent chemical heterogeneity in the lower mantle.

Key words: array, core–mantle boundary, *P* waves, scattering.

INTRODUCTION

The lowermost mantle close to the core–mantle boundary has long been recognized as structurally anomalous from a seismological perspective (e.g. Gutenberg 1913); more recently Lay & Helmberger (1983) documented a discontinuity approximately 300 km above the core–mantle boundary, at the top of the D″ region. Since that time there have been more observations suggesting that a discontinuity close to this depth exists (e.g. Houard & Nataf 1992; Kendall & Shearer 1994; Freybourger *et al.* 1999), but there is still uncertainty as to whether this is a global feature (Nataf & Houard 1993). Indeed, there is increasing evidence for the discontinuity being intermittent. For example Kendall & Nangini (1996) found no evidence for a discontinuity beneath parts of the Caribbean, and similarly Vidale & Benz (1993) observed none beneath the northern Pacific. Other studies, such as that of Garnero *et al.* (1988), provide evidence for a discontinuity which disappears laterally, or represents a coalescence of discrete objects locally into a layer (Gaherty & Lay 1992). More recently, evidence for small-scale heterogeneity throughout the mantle was proposed by Hedlin *et al.* (1997). Small isolated scattering bodies have recently been detected both in shallower regions of the lower mantle (Kaneshima & Helffrich 1998) and close to the core–mantle boundary (Thomas *et al.* 1999). This evidence is reflected in recent models of Earth structure, which are moving away from the traditional 'layer-cake' model and are perhaps better described as 'marble-cake' models (e.g. Helffrich & Wood 2001). A real Earth, which is laterally heterogeneous and chemically unstratified, is quite different from traditional models in the dynamic behaviour of slab subduction into the lower mantle and ascent of mantle plumes, because radial compositional barriers do not exist to impede advection of material. Strengthening the observational basis for this view is an important step in resolving the debate concerning the Earth's convective style and chemical make-up.

This study attempts to characterize the small-scale variability of the lower mantle and interpret it in the context of the subduction and melting processes, which may produce chemical heterogeneity. Using short-period array data we probe the core–mantle boundary (CMB) region beneath Nova Scotia in the North Atlantic. Previous studies in this area have produced conflicting verdicts on the presence of the D″ discontinuity. Both Houard & Nataf (1992), with *P* waves, and Kendall & Shearer (1994), with *S* waves, found evidence for a lower mantle reflector in this region. Kendall & Shearer (1994) tentatively estimated the height of this reflector to be 200–300 km above the CMB. However, Weber & Körnig (1990, 1992) specifically identified this region as an area of non-observations for a precursory signal to *PcP*. Tomographic images using both *P* waves (van der Hilst *et al.* 1997) and *S* waves (Grand *et al.* 1997) contain areas of fast wave speeds at depths close to the core–mantle boundary in this area. However, with lateral resolution of the order of hundreds of kilometres, such images can only ever provide evidence of large-scale general features, and our interest lies in the smaller-scale heterogeneous structure.

*Now at: QinetiQ Ltd, Malvern Technology Centre, St Andrew's Road, Malvern, Worcestershire WR14 3PS, UK. E-mail: lpbrana@qinetiq.com

Results from this study provide conclusive evidence for small-scale lower mantle structure in this region and suggest that it is a consequence of scattering rather than interaction with a large-scale discontinuity. Though the precise nature of this scattering body is debatable, its seismic signature is clear and demonstrates that small-scale heterogeneity exists at the base of the mantle.

DATA

Records from the UK array of short-period stations (Fig. 1a) constitute the data we use to characterize the scattering. Later analysis also includes data for specific events recorded at European broadband stations (Fig. 1b). The data were digitized from analogue tape records or taken from digital records (after 1996). Events were chosen on the basis of magnitude (>5.5 M_b) and location (between 5°N and 25°N of latitude, and 250°E and 280°E longitude) (Table 1). Seismic traces not rejected as a result of high noise levels were bandpass filtered between 0.2 and 4 Hz, and a consistent feature in the *P* arrival was picked manually. In total, seven events were found to contain a precursory signal (henceforth called *X*) to *PcP*, mainly from the Guerrero region of Mexico (Fig. 2).

Source locations were derived from the EHB catalogue (Engdahl *et al.* 1998). For the most recent event, for which EHB data were unavailable, the information about the source location was obtained from the National Earthquake Information Centre. Traveltimes of later arriving phases were calculated using the AK135 velocity model (Kennett *et al.* 1995).

METHODS

Time versus slowness stacks

In order to obtain accurate estimates of *X* slowness and time lag, relative to *P*, a standard slant-stacking technique was applied (Vidale & Benz 1992). Summation of the stacked traces increases the signal-to-noise ratio and thus enhances the presence of any small, coherent signals. *N*th-root stacking was applied (Muirhead 1968; McFadden *et al.* 1986) to identify scattering, and linear ($N = 1$) stacks used to measure amplitude relative to direct *P*.

Slowness versus azimuth stacks

Standard slant-stacking methods, like that described above, assume that all signals travel along paths with the same backazimuth. While this may apply to a spherically symmetrical Earth, it is unlikely to be an appropriate assumption for scattered signals, produced as a result of a laterally heterogeneous real Earth (Weber & Wicks 1996; Kaneshima & Helffrich 1998). Azimuth deviations are searched for using a slowness versus azimuth array-stacking technique. These stacks are obtained by rotating the array by small angles and

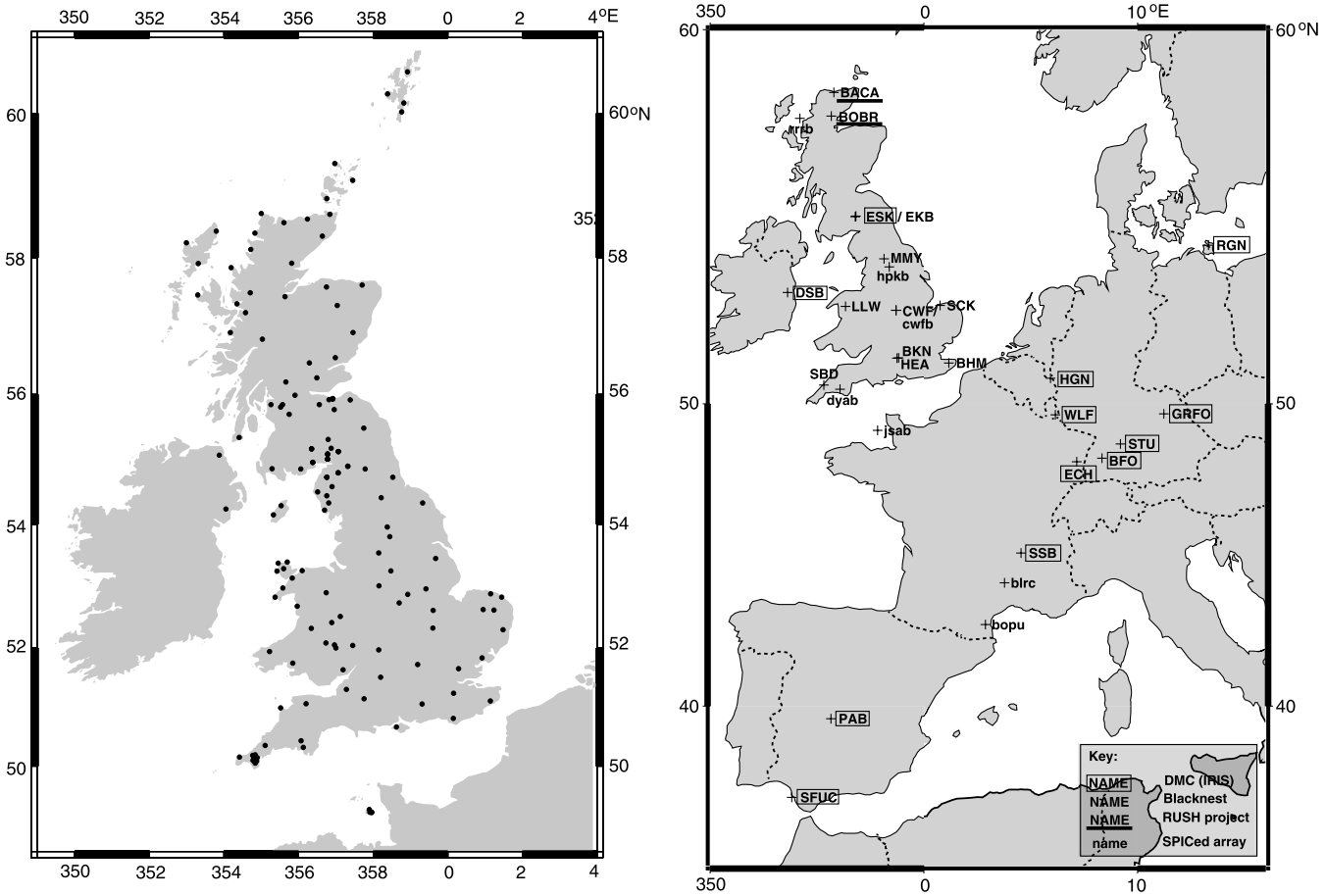

Figure 1. (a) Map showing the UK array of short-period stations. There are around 150 stations in total, although not all provided data for this study. (b) Locations of broadband stations used in this study. The scattered phase could be clearly observed in the broadband records of all of these stations, even though they cover a large geographical area.

Table 1. Central American events in which a *PcP* precursor could be clearly observed.

Date (yr/month/d)	Source	Origin time (hh:mm:ss.ss)	Latitude (°N)	Longitude (°E)	Depth (km)	Mag. (M_b)	Locality
1993/10/24	EHB	07:52:18.26	16.77	−98.73	28.0	6.3	Near coast,
	NEIC	07:52:15.63	16.75	−98.72	20.0		Guerrero, Mexico
1994/07/04	EHB	21:36:43.64	14.94	−97.28	15.0	6.1	Off coast,
	NEIC	21:36:41.96	14.89	−97.32	14.0		Oaxaca, Mexico
1994/12/10	EHB	16:17:40.39	18.11	−101.40	52.0	6.6	Guerrero, Mexico
	NEIC	16:17:38.51	18.14	−101.38	48.0	6.6	
1997/05/22	EHB	07:50:53.82	18.65	−101.64	60.0	5.8	Guerrero, Mexico
	NEIC	07:50:53.52	18.68	−101.60	70.0		
1998/04/20	EHB	22:59:16.92	18.56	−101.10	71.5	5.9	Guerrero, Mexico
	NEIC	22:59:14.77	18.52	−101.20	67.0		
1999/12/29	EHB	05:19:45.58	18.18	−101.44	69.0	6.1	Guerrero, Mexico
	NEIC	05:19:46.91	18.24	−101.43	69.0	6.1	
2000/07/21	NEIC	06:13:41.33	18.41	−98.92	80.0		Guerrero, Mexico

EHB sources are from the Engdahl, van der Hilst and Buland catalogue (Engdahl *et al.* 1998), while NEIC denotes locations from the PDE catalogue of the National Earthquake Information Centre.

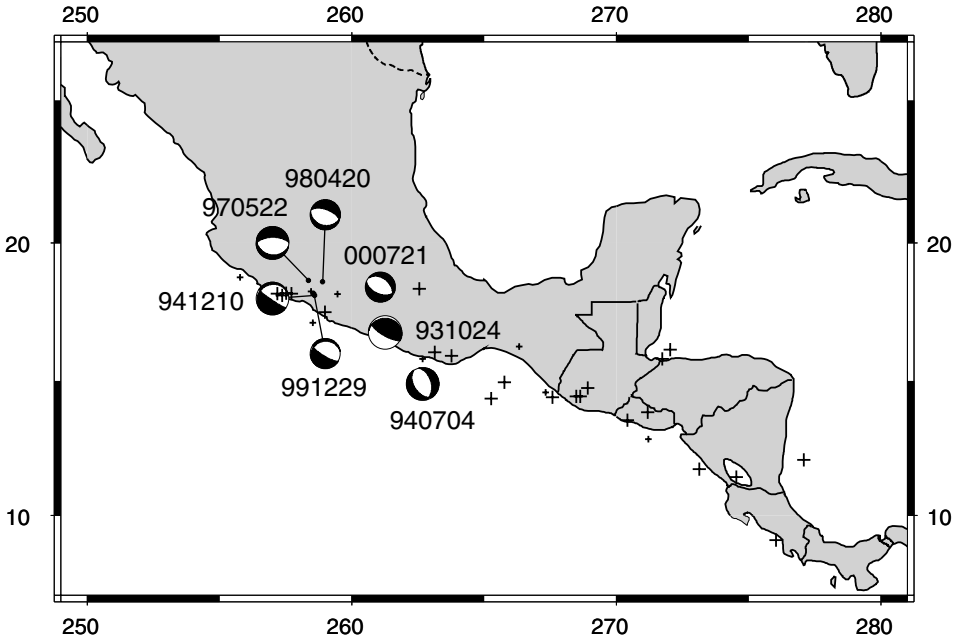

Figure 2. The locations of events analysed in this study. The seven events with focal mechanisms (Dziewonski *et al.* 1981) are those in which a scattered signal could be observed. Large crosses denote the locations of events in which a scattered signal could not be observed, while small crosses mark the locations of events in which scattering may be masked by low signal-to-noise ratios or inadequate data.

summing energy within 2 to 3 s time windows, corresponding to the estimated duration of X (Kaneshima & Helffrich 1998).

Ellipsoids of scattering

Isochrons which delineate the boundaries of possible scattering locations for various traveltimes of X relative to P are roughly elliptical in shape and thus are called scattering ellipsoids. Contours are calculated given the scattered wave traveltime, and scattering type (P–P; S–P). A grid of latitudes, longitudes and depths, near the lower mantle ray path, is searched to determine the possible locations of scatterers which are feasible, given the observed travel time delay relative to P.

Joint likelihood of scattering

A joint likelihood calculation is a probabilistic determination based on a number of independent observations. In the case of imaging scattering within the mantle, slant-stacking techniques are used to observe traveltime and relative slowness of the phase. In addition, the azimuth-slowness stack provides backazimuth deviations relative to the P wave, for the desired phase. These are then combined to determine the most likely location of the source of the arrival (Scherbaum *et al.* 1997; Kaneshima & Helffrich 1998). The area to be analysed is treated as a grid of 'potential' scattering points. For each gridpoint, a 'likelihood' (or relative probability), P_x, is individually computed for each earthquake, before being multiplied together to obtain the joint scattering likelihood for that particular point given all observations. The joint likelihood is therefore defined

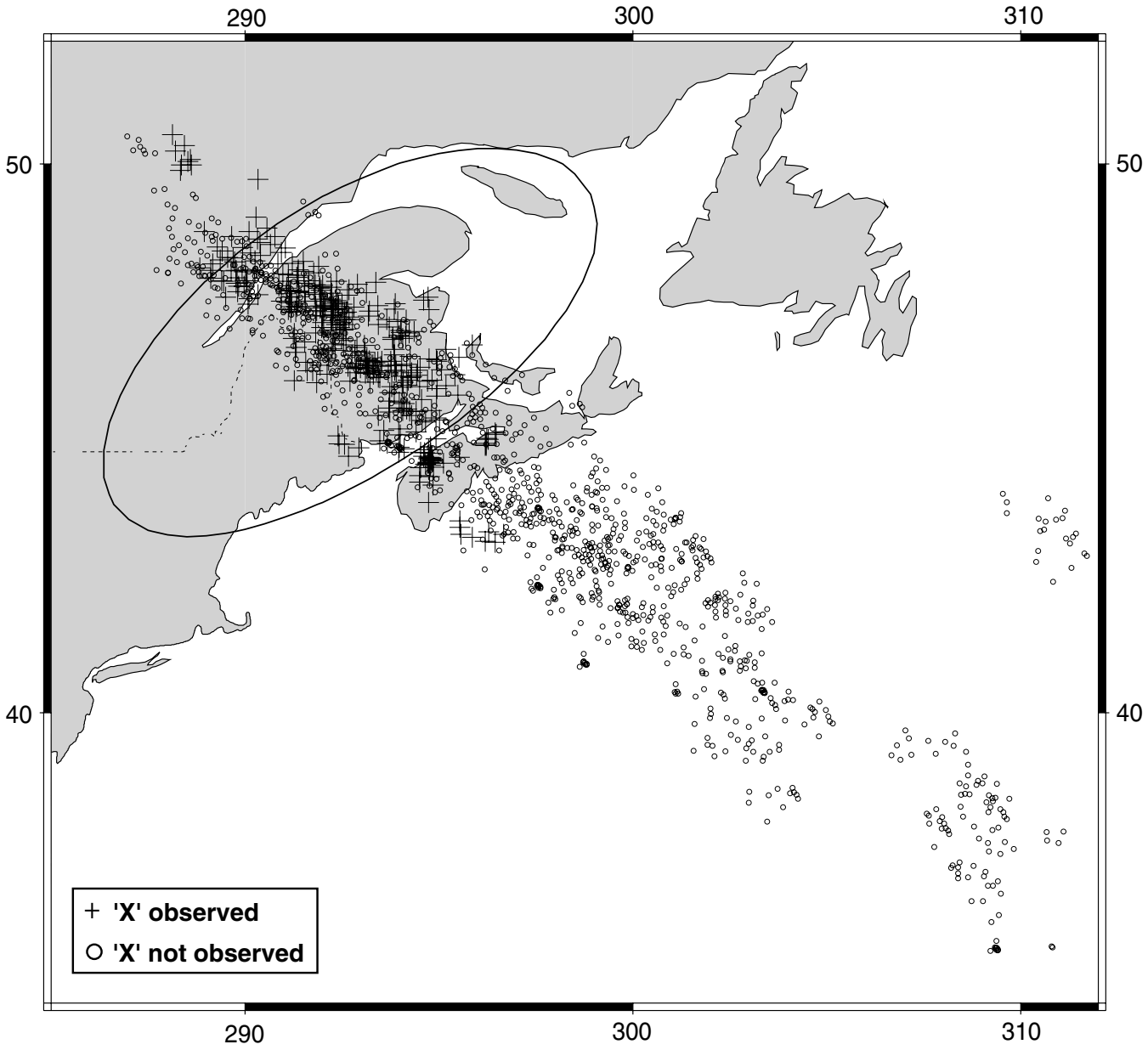

Figure 3. Map displaying the theoretical bounce points of *PcP* for both events where the scattered wave could and could not be observed. Assuming that the scattered signal travels along the same azimuth as *P* and *PcP* this suggests the likely location and extent of the scattering region. Observation versus non-observation decisions were made on a per event, rather than individual seismogram, basis. The Fresnel zone (l/4) at a dominant period of 2 s is shown for event 991229.

as (Kaneshima & Helffrich 1998):

$$P_x = \prod_i \exp\left(-\frac{(p_i - p_{o,i})^2}{\varepsilon_p^2} - \frac{(\mathrm{baz}_i - \mathrm{baz}_{o,i})^2}{\varepsilon_{\mathrm{baz}}^2} - \frac{(t_i - t_{o,i})^2}{\varepsilon_t^2} \right) \quad (1)$$

where p_i, p_{oi}, baz_i, baz_{oi}, t_i, t_{oi} are the calculated and observed values of slowness, backazimuth and traveltime respectively, for the *i*th source–array pair. ε_p, $\varepsilon_{\mathrm{baz}}$ and ε_t are the uncertainties in each measurement—in this study, 0.2 s deg^{-1}, 1.0° and 0.5 s respectively. It should be noted that as stated the probability P_x is a relative probability only and therefore does not provide the absolute probability of scattering, just the most likely position of a scatterer given that it is already known to exist.

RESULTS

Observations versus non-observations

Fig. 3 shows a map of the theoretical bounce points of *PcP* for events for both observations and non-observations of *X*, and a typical Fresnel zone for a dominant period of 2 s. Non-observations of *X* were obtained from 22 events from the same region. It should be noted that observation versus non-observation decisions were made on a per event, rather than individual seismogram, basis. Events with low signal-to-noise ratios or long *P* wave trains were not included, especially those events for which only a small number of records were available. While the theoretical bounce points of events where the *PcP* precursor is observed are clearly clustered in the northwest

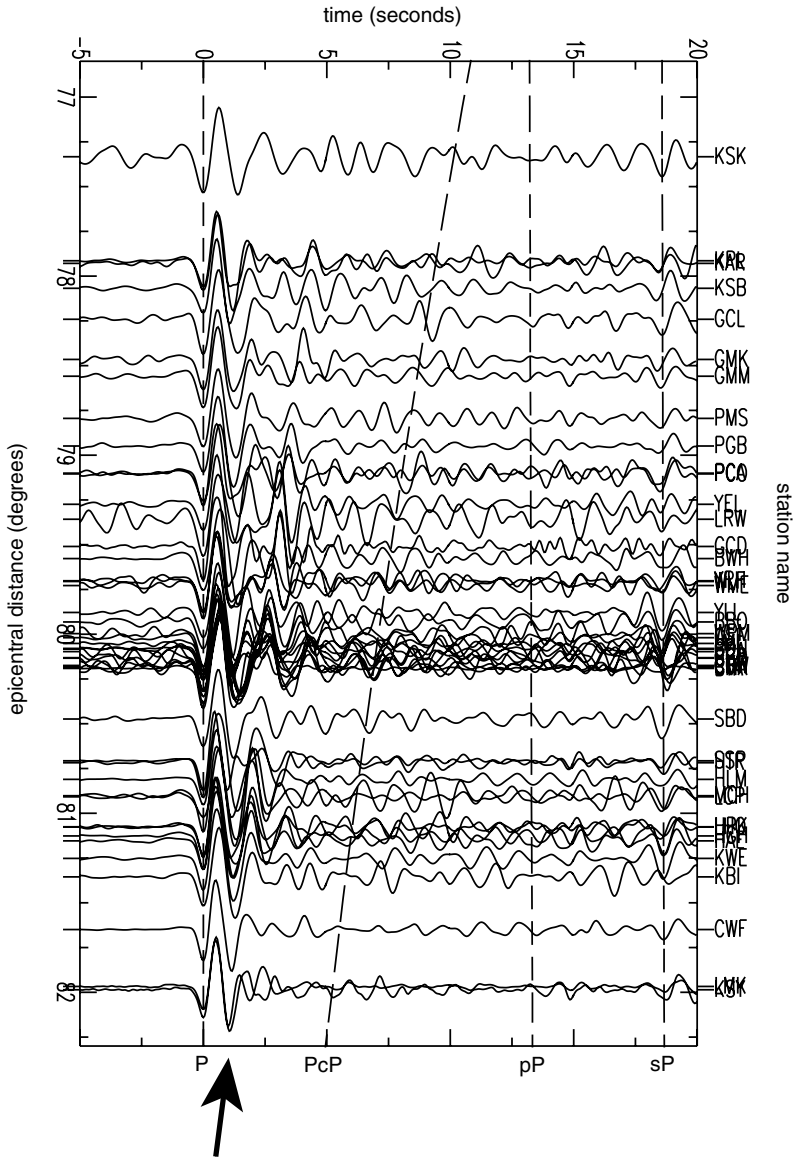

Figure 4. Record section of *P*-aligned waveforms for event 931024. The arrow denotes the onset of the scattered signal. The relative amplitude of the scattered signal to *P* varies throughout the array, in no obvious systematic manner. Indeed in some records it is difficult to observe the signal at all.

region, there is no other discernible pattern to these observations, particularly in the region of bounce points which includes both the observations and non-observations.

However, it should be noted that even for events where *X* can clearly be observed, it is not always visible in the records from each station of the array (Fig. 4). Indeed *PcP* itself is not always visible in both the record sections and slant stacks (see Fig. 5). In Fig. 4 the scattered phase clearly occurs before the theoretical arrival time of *PcP* at these distances. The moveout of the signal across the array is very similar to that predicted for *PcP*, suggesting that the wave takes off in a downward direction and may possibly travel along a path similar to *PcP*. Since the signal is visible in a large number of stations across the array, it is unlikely to be a product of near-receiver structure.

Slowness and azimuth deviations

Observations of slowness, traveltime and azimuth deviation, relative to *P* (summarized in Table 2) were derived from vespagrams (time versus slowness slant stacks, contoured as fractions of the maximum power) (Fig. 5) and azimuth versus slowness stacks of the scattered phase (Fig. 6). Uncertainty estimates are derived from the 0.8 contour level in linear stacks for both stacking techniques. The relative slowness of the precursor is in each case negative relative to *P*, and ranges between -0.62 and -0.85 s deg^{-1}. Small azimuth deviations suggest that the source of *X* may lie slightly away from the direct ray path from the source to the receiver.

Joint likelihood of scattering

Joint likelihood calculations were performed based on *P* to *P* scattering. While *S* to *P*, *pP* to *P* and *sP* to *P* scattering may theoretically occur in near-source locations, the combined traveltime, backazimuth and relative slowness observations cannot be satisfied together. In particular, locations which approximately satisfy the backazimuth and receiver slowness requirements for scattered waves result in traveltimes much longer than observed (as much as 100 s greater).

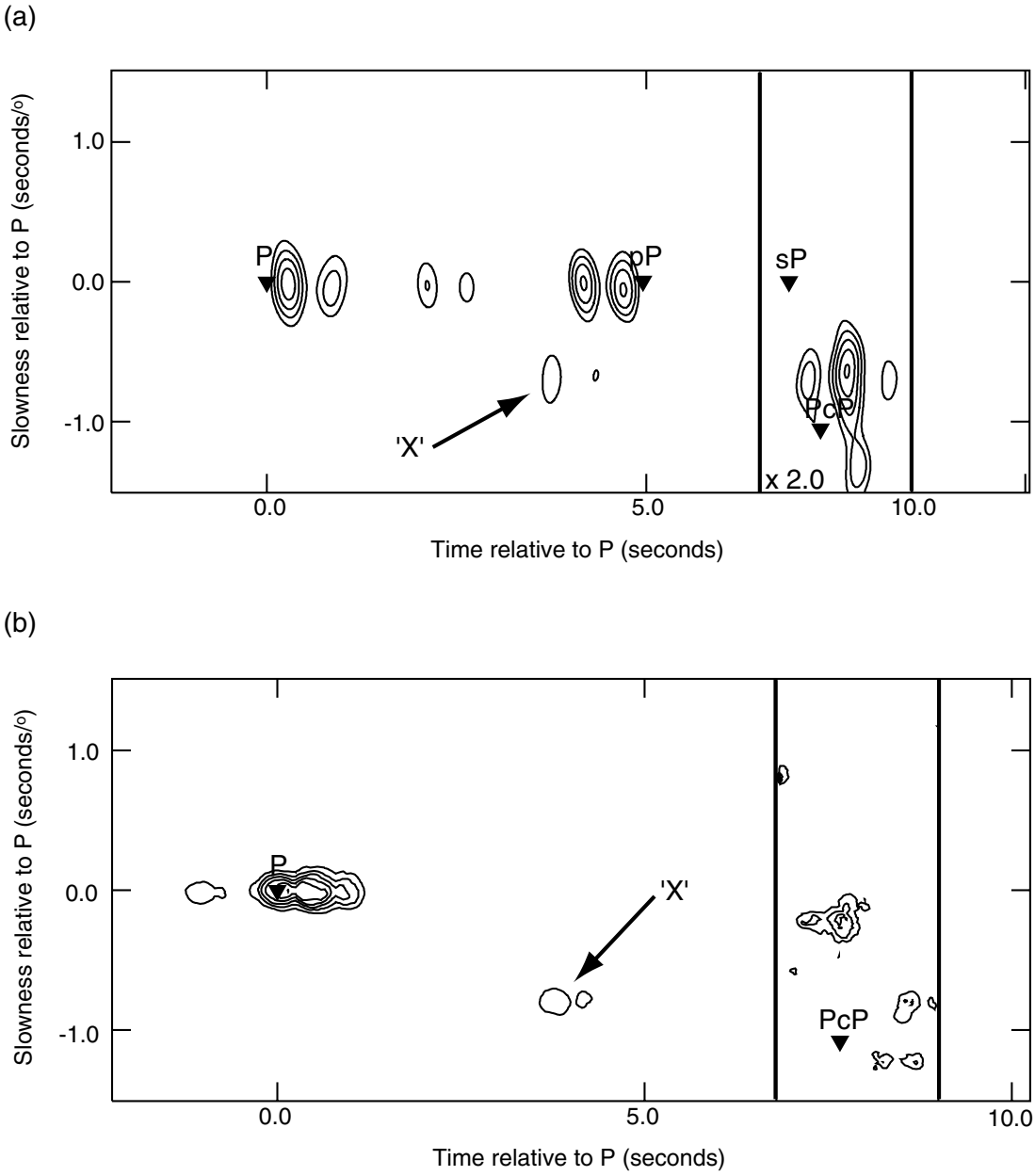

Figure 5. Vespagrams to determine the relative slowness and time lag of the scattered phase. Stacking slowness interval is 0.01 s deg^{-1}. Triangles denote the theoretical arrival times of later phases, while arrows point to the scattered signal. Slowness and lag time estimates are derived from the 0.99 contour, while uncertainty estimates are based on the 0.8 contour level. Areas between the two vertical lines have been magnified by the amounts shown. (a) A linear stack of event 940704: contours are 0.6, 0.7, 0.8, 0.9 and 0.99 of the maximum power. (b) A cube root stack of event 931024: contours are 0.2, 0.3, 0.4, 0.5, 0.6, 0.7, 0.8 and 0.99 of the maximum power.

The most likely location for scattering was determined for each source–array pairing individually, as well as combining these probabilities together. When the source–array pairs were used to calculate a joint probability (eq. 1), the maximum value occurred at 44.0°N, 71.5°W and 2720 km depth (Fig. 7).

For individual events the maximum probability value ranged from 0.302 to 0.985 (Fig. 8a). While for most of the events the locations cluster close together, two events have locations which are spread further away. This may be an artefact of the ambiguity associated with assigning a scatterer position based only on traveltime (Fig. 8b), but it may also delineate particular specular reflections of a larger body. We examine this possibility later.

DISCUSSION

Scatterer or discontinuity?

In the joint likelihood calculation made above results show a clear maximum likelihood for X. To determine whether it is due to a horizontal reflector or a point scatterer we review the relevant theory for elastic scattering in an exponentially correlated medium (Wu & Aki 1985a,b). P to P scattering amplitudes have a characteristic frequency squared dependence at low frequencies. When variations in elastic constants λ and μ and density ρ are identical ($\delta\lambda/\lambda = \delta\rho/\rho = \delta\mu/\mu$), amplitudes are independent of this relationship at

Table 2. Observations of traveltime, slowness, azimuth deviation and amplitude relative to *P*, of the scattered signal.

Event date (yr/month/d)	Relative traveltime (s)	Relative slowness (s deg^{-1})	Azimuth deviation (deg)	Relative amplitude (per cent)	Amplitude uncertainty (per cent)	Scattering angle (deg)
1993/10/24	+4.60	−0.62	+0.12	−37	6	14.53
1994/07/04	+3.60	−0.60	+0.25	−70	6	14.14
1994/12/10	+5.00	−0.80	+0.52	30	1	12.71
1997/05/22	+5.20	−0.85	−1.98	47	6	14.38
1998/04/20	+3.90	−0.78	−0.10	52	8	14.14
1999/12/29	+2.70	−0.80	+0.55	36	3	13.22
2000/07/21	+5.95	−0.68	+0.11	79	5	16.10

For each event, the uncertainties in each measurement are 0.5 s, 0.2 s deg^{-1} and 1.0 deg respectively. While traveltime certainly varies as a function of epicentral distance, a single fixed value is obtained from linearly stacked waveforms and represents a traveltime to the centre of the array. Relative amplitudes are determined from envelope waveforms of linearly stacked short-period waveforms. Uncertainties in relative amplitude are calculated separately for each event, and are based on linearly stacked waveforms at slowness values between the estimated errors. Values range between ±0.01 and ±8 per cent. Scattering angles are calculated for a scatterer at 44.0°N, 71.5°W, 2720 km depth.

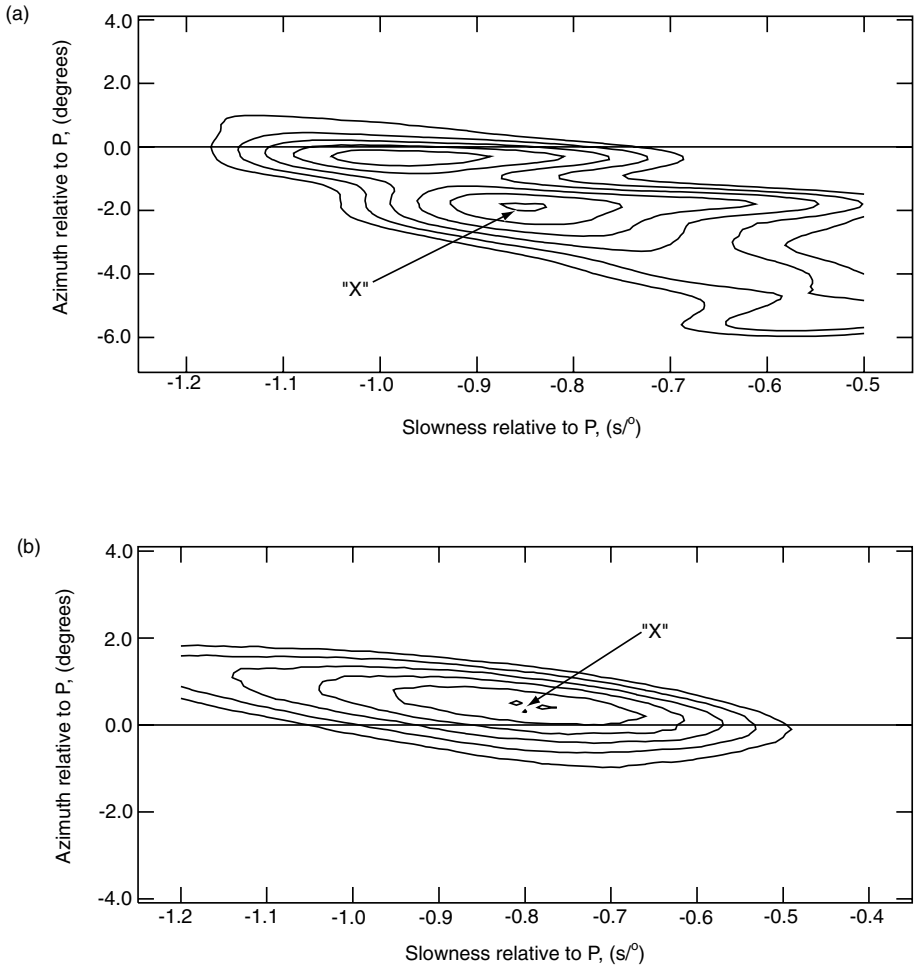

Figure 6. Azimuth versus slowness stacks: (a) linear stack ($N = 1$) of event 970522; (b) cube root stack ($N = 3$) of event 941210. Stacking slowness interval is 0.01 s deg^{-1} and azimuth stacking interval is 0.1°. The time window of stacking is between 1 and 2 s and depends on the length duration of the scattered signal in the corresponding vespagram. The horizontal line denotes zero azimuth deviation—signals centred on this line would have travelled along the same azimuth as *P*. Contours in each case are 0.5, 0.6, 0.7, 0.8, 0.9 and 0.99 of the maximum power. Observations of azimuth and slowness deviation were obtained from the 0.99 contour, while uncertainties were derived from the 0.8 contour level.

high frequencies above $K \approx 1$, a characteristic non-dimensional frequency:

$$K = \frac{2\pi f}{V_0} a. \tag{2}$$

Here a is the correlation distance, V_0 is the ambient *P*-wave speed and f is frequency. Spectral division of the scattered wave by the direct *P* wave will reveal these features if they exist. Unlike *S* to *P* scattering, there is no need to correct for different attenuation between the source and the scatterer (Kaneshima &

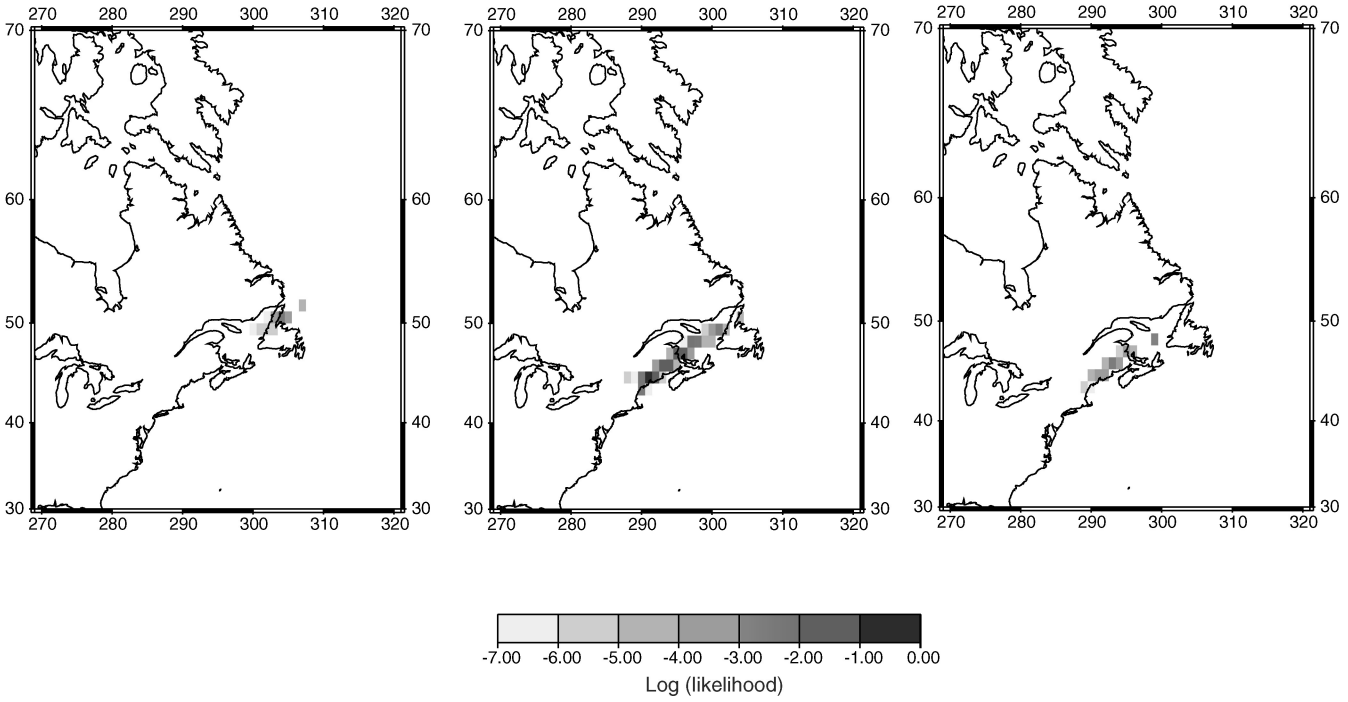

Figure 7. Joint likelihood of *P-P* scattering at three depths (left 2680 km, centre 2720 km, right 2760 km). Values in each grid are normalized to the overall maximum at 44.0°N, 71.5°W and shading denotes logarithmic likelihood values.

Helffrich 1999), nor is there significant uncertainty due to radiation pattern.

Fig. 9 displays the result of the spectral division of X by P, obtained from linear stacks, made at an appropriate relative slowness, of unfiltered broadband data recorded at UK and European stations (including the temporary SPICeD array (Kendall & Helffrich 2001, Fig. 1b). In Fig. 9, at low frequencies the relationship is approximately f^2. Since this follows the expected relationship for scattering it seems appropriate to treat this signal as a result of scattering rather than reflection or refraction from a first-order discontinuity, which would have no frequency dependence in the ray approximation.

Scatterer sizes and positions

For a medium with $\delta\lambda/\lambda = \delta\rho/\rho = \delta\mu/\mu$, Wu & Aki (1985a) showed that the transition between the high- and low- frequency behaviour for P to P scattering occurs at:

$$f = \frac{V_0}{2\pi a} \tag{3}$$

where f is frequency, V_0 is velocity and a is the correlation distance. The spectral knee, at 3.0–3.5 Hz (Fig. 9) suggests a correlation distance of 0.6–0.7 km, assuming a P velocity of 13.62 km s^{-1} at 2720 km depth (derived from the AK135 velocity model). However, there is little, if any, signal visible in the amplitude spectra of individual broadband stations at frequencies greater than 2.0–3.0 Hz. Thus, 0.6–0.7 km represents a lower bound on the characteristic scatterer size within a potentially larger scattering region.

Assuming that the region is large enough for the specular reflection to approximately obey Snell's law, we can estimate the geometrical orientation of the surface of the scattering region (as later analysis shows, the scattering region size justifies this assumption). This can be calculated by finding the orientation of the plane yielding a P to P reflection, taking into account source and receiver slowness as well as the azimuth from the scatterer to the source and receiver. Using a 'mean' event location of 18.38°N, 101.30°W and 57.13 km depth, with the centre of the UK array at 54.54°N, 3.52°W, the scattering surface appears to dip at angle of ∼11.8° along an azimuth of ∼ −8.5°N.

Constraints on scatterer properties

Velocity changes

Table 2 also provides estimates of the relative amplitude of the scattered phase to direct P, measured from linearly stacked envelopes of records for each event. Amplitudes of the scattered phase vary greatly from 30 to 70 per cent and have both normal and reversed polarities relative to P. A crude way to estimate the contrast in properties between the scattering body and the mantle is to treat it as a planar interface. This contradicts the observation that scattered wave amplitude is proportional to f^2, but it provides an upper bound on the possible velocity contrast. Fig. 10 shows the feasible range of δVp, δVs and $\delta\rho$ perturbations to AK135 wave speeds that yield amplitudes of the scattered wave relative to P, given the planar geometry deduced above. Even with the wide range in relative amplitudes observed, the graphs show that nearly all the events have fields which overlap. There are no real constraints on density, but $\delta Vs/Vs$ variations are 1.4 to 6.6 per cent and $\delta Vp/Vp$ variations are 0.4 to 0.7 per cent. (Amplitudes for 931024 are discrepant with respect to $\delta V/V$ for the other events.) This relative increase is much smaller than other estimated P velocity changes across D″ which are of the order of 2.0–3.0 per cent (Wysession *et al.* 1998), although Krüger *et al.* (1995) suggest that P velocity changes of ∼ +0.5 per cent may be acceptable if the discontinuity is sharp. S-wave speeds, however, are in the range of ≤3 per cent as reported elsewhere (e.g. Weber & Davis 1990; Kendall & Nangini 1996; Lay & Young 1996).

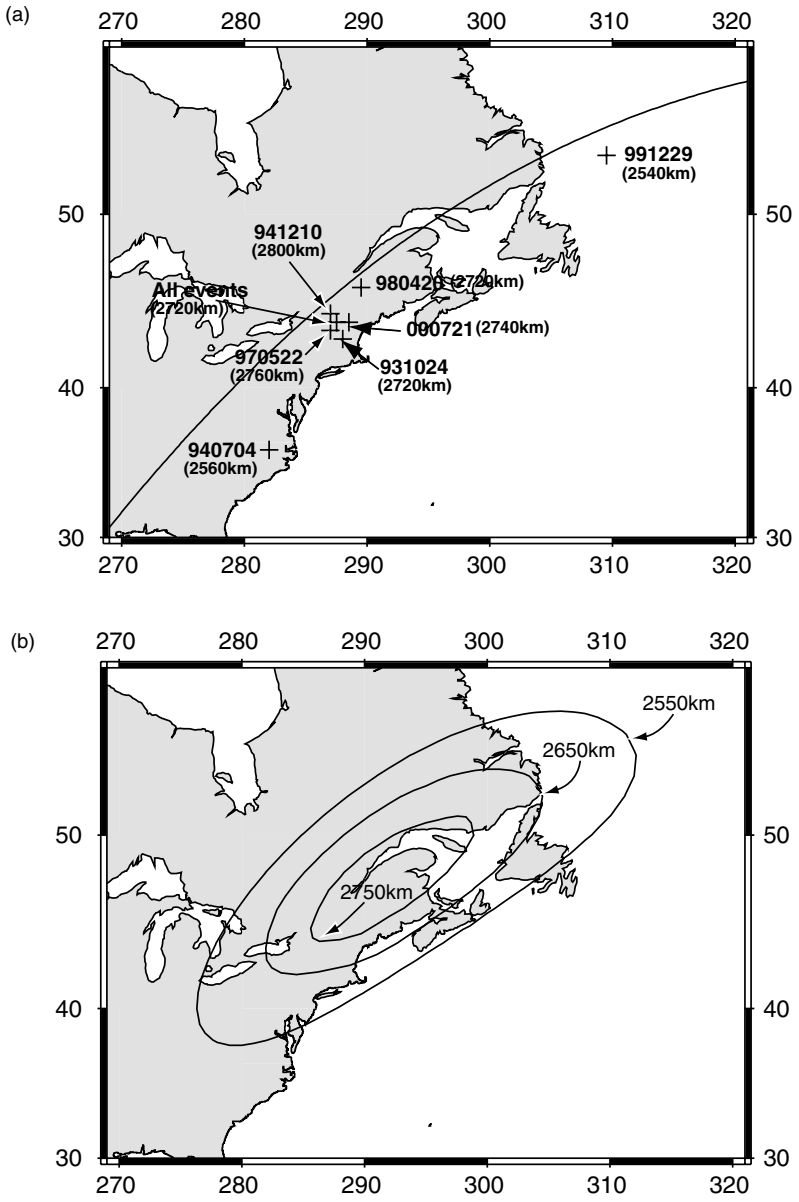

Figure 8. (a) Locations of the most likely scatterers for each individual source–array pair. For reference, the curved line denotes the great circle path of event 991229. (b) Isochrons (in this case for a lag time of ∼5 s with respect to *P*), at three different depths, for event 980420. As depth increases the range of possible scatterer locations decreases for a fixed lag time, so that in 3-D the scattering isochrones appear to have an ellipsoidal shape.

Scattering region size

Table 2 shows the observational data relating scattered energy and the scattering geometry, calculated from ray geometry and assuming that the scattering location lies at 44.0°N, 71.5°W, at a depth of 2720 km. For the events containing the scattered phase, their scattering angles range between 12.7° and 16.1°. Wu & Aki (1985a,b), show through elastic wave scattering theory that the scattering angle, θ, is related to the directional scattering coefficient, g^{PP}, by:

$$g^{PP}(\theta) = 2\frac{\omega^4}{V_0^4}a^3\,{}^PR^P(\theta)\frac{1}{\left[1+(2\langle\omega/V_0\rangle a\sin\langle\theta/2\rangle)^2\right]^2} \tag{4}$$

where ω is angular frequency, V_0 is the ambient velocity and a is the correlation distance. If θ is small (which is the case in this study—see Table 2), then the denominator in eq. (4) is approximately 1.0. This means that the scattering coefficient depends on $(\omega^4/V_0^4)a^3$, and ${}^PR^P(\theta$, where ${}^PR^P(\theta)$, the directional scattering factor, is determined by:

$$\begin{aligned}{}^PR^P(\theta) = &\left\langle\left(\frac{\delta Z_\alpha}{Z_{\alpha 0}}\right)\right\rangle^2\left(\cos\theta-\frac{1}{3}-\frac{2}{3}\cos^2\theta\right)^2\\ &+\left\langle\left(\frac{\delta V}{V_0}\right)\right\rangle^2\left(\cos\theta+\frac{1}{3}+\frac{2}{3}\cos^2\theta\right)^2\\ &-2\left\langle\frac{\delta Z_\alpha}{Z_{\alpha 0}}\frac{\delta V}{V_0}\right\rangle\left(\cos\theta-\frac{1}{3}-\frac{2}{3}\cos^2\theta\right)\\ &\times\left(\cos\theta+\frac{1}{3}+\frac{2}{3}\cos^2\theta\right)\end{aligned} \tag{5}$$

where $\delta Z_\alpha/\delta Z_{\alpha 0}$ is the *P*-wave impedance perturbation and $\delta V/V_0$ is the velocity perturbation. At a characteristic scattering angle of 15° (Table 2), the contributions from each term are, respectively,

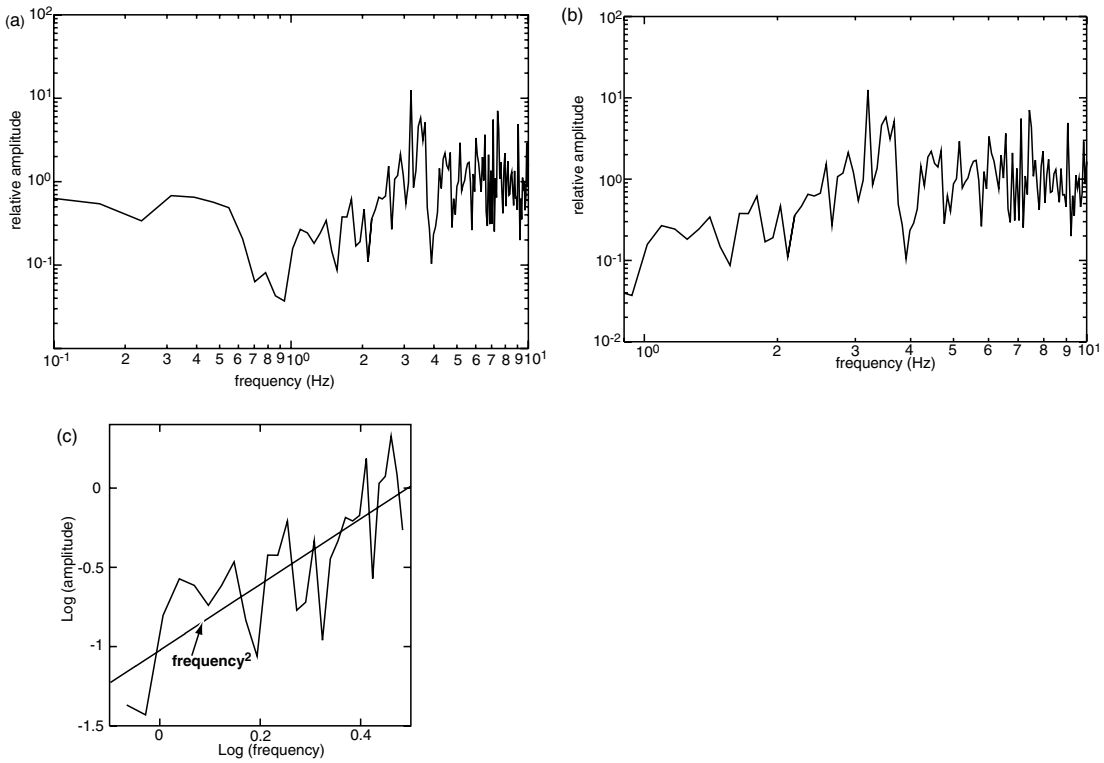

Figure 9. (a), (b) Spectra of X/P. The scale is logarithmic. Note the low gradient slope between approximately 0.9 and 3 Hz with a knee in the spectra at approximately 3–3.5 Hz, followed by a plateau. (c) A line of best fit between frequency and amplitude at low frequencies (in this case 0.9–3.0 Hz) has a slope of 2.06742 ± 0.32 and an intercept of -1.02107 ± 0.098.

$O(10^{-7})$, $O(10^{-3})$ and $O(10^{-8})$, so we retain only the second. Strictly, the unequal *P*- and *S*-wave speed perturbations, derived earlier from the planar interface approximation, violate the assumptions inherent in eq. (5). Within the bounds they set, however, eq. (5) is applicable.

The scattering region size can now be constrained since the directional scattering coefficient only depends on:

$$g^{PP}(\theta) = 2\frac{\omega^4}{V_0^4}a^3\left\langle\left(\frac{\delta V}{V_0}\right)^2\right\rangle\left(\cos\theta + \frac{1}{3} + \frac{2}{3}\cos^2\theta\right)^2. \quad (6)$$

To relate this to the observed scattered wave amplitude, we use the relation from Wu & Aki (1985a):

$$g^{PP}(\theta) = \frac{4\pi r^2}{L^3}\left(\frac{A}{A_0}\right)^2. \quad (7)$$

where r is the distance between the receiver and the scatterer, L is the scattering region size and (A/A_0) is the observed scattered wave amplitude ratio (Table 2), accounting for geometric spreading of the incident wave at the scatterer (which reduces it by 1/5 for our geometry). Combining eqs (6) and (7), the quantity L^3 should be constant:

$$4\pi r^2\left(\frac{A}{A_0}\right)^2\frac{1}{\langle(\delta V/V_0)\rangle^2(\cos\theta + 1/3 + 2/3\cos^2\theta)^2} = L^3. \quad (8)$$

For a characteristic frequency of 0.4 Hz (estimated from individual broadband spectra, which range from 0.2 to 0.6 Hz), V_0 of 13.62 km s^{-1}, a mean value of $\delta V/V_0$ of 0.55 per cent, a correlation length a of 0.6 km and a radius r of 4260 km (estimated from ray tracing, given the scatterer location), we obtain an average L^3 of 3.281×10^8 km^3. Thus, the scattering region size length, L, is approximately 690 km. This is roughly in agreement with the spatial distribution of individual scattering locations (∼500 km × 400 km), and the size of the Fresnel zone (∼400 km × 400 km at the core–mantle boundary), (Fig. 3).

Thermal perturbations

Temperature anomalies are related to density anomalies through the thermal expansivity of the particular pressure–temperature regime such that:

$$\delta T = -\frac{\delta\rho/\rho}{\alpha} \quad (9)$$

where δT is the temperature anomaly, ρ is the density and α is the thermal expansivity which has a value of 1×10^{-5} K^{-1} in the lower mantle (Chopelas & Boehler 1992). Possible density jumps of 1 to 60 per cent (Revenaugh & Jordan 1991) would thus equate to temperature anomalies between 1000 and 60 000 K. A density anomaly of between 1 and 3 per cent could represent either partial melting or chemical heterogeneity. Anomalies larger than 3 per cent require chemical heterogeneity since this would exceed the estimated solidus temperature at the base of the mantle (Zerr *et al.* 1998), and the upper bound of 60 per cent is much greater than the melting temperatures of lower mantle constituents (Boehler 2000).

What is D″?

D″ has long been suspected as the location of a 'graveyard' for subducted slabs—could our scatterer represent a portion of such a slab? Engebretson *et al.* (1992) reconstruct the possible locations of ancient subducted slab material through the Mesozoic under the North

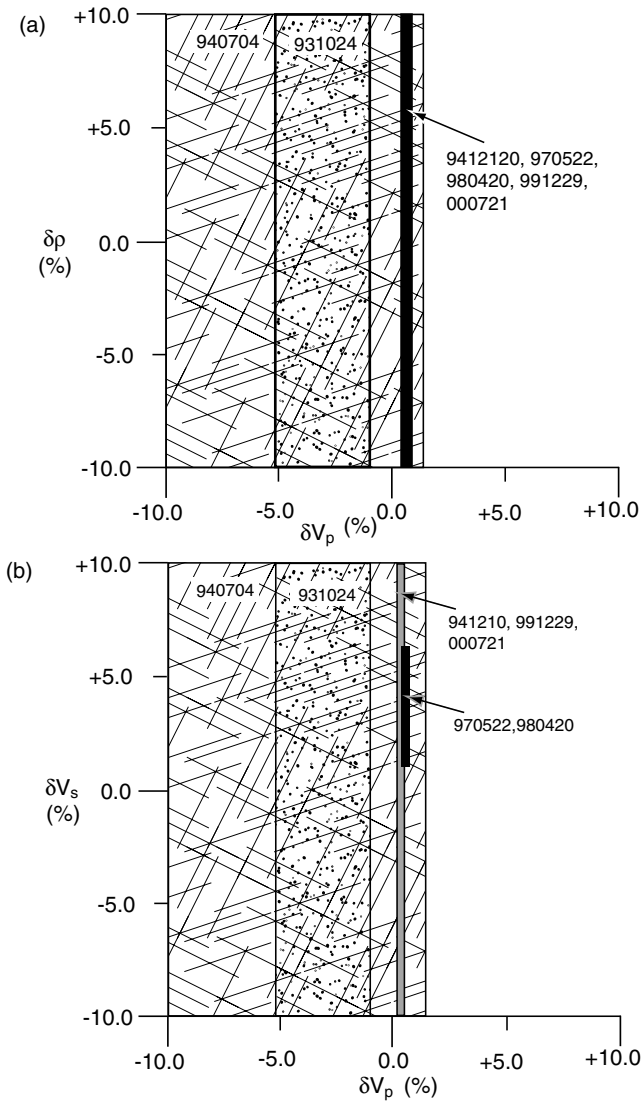

Figure 10. Constraints on velocity and density changes relative to ambient determined from estimates of the relative amplitude between *P* and *X* via plane-wave conversion coefficients. The relative amplitudes were estimated from linear stacks of short-period data, while Zoeppritz's equation (Young & Braile, 1976) can be used to estimate the relationship between amplitude, velocity and density: (a) δVp versus $\delta\rho$; (b) δVp versus δVs. In each case, δVp is better constrained than both $\delta\rho$ and δVs. While the range of possible velocity and density changes are shown here up to ± 10 per cent, in tests, both δVs and $\delta\rho$ displayed ranges as great as ± 50 per cent.

Atlantic. Using slab descent rates inferred from recent subduction rates, Grand (1994) suggests that slabs subducted approximately 130–140 Ma may lie at a depth close to the core–mantle boundary. The reconstructions by Engebretson *et al.* (1992) for this time place subducted slab material beneath Nova Scotia, suggesting that the scattering region may be a chemical heterogeneity within the slab dregs. We can strongly discount partial melting because the velocity perturbation is positive suggesting cooler rather than hotter material, and it would be impossible to heat only small portions of the subducted slab material by heat conduction from the core. The scatterers cannot be cool, disaggregated subducted crust because thermal equilibration within the lower mantle (with a thermal diffusivity of $\sim 1 \times 10^{-6}$ m^2 s^{-1}) will occur on timescales of 10 to 100 Myr, which is less than the age of the material. Predictions of thermochemical velocity changes in the presence of a slab at the base of the mantle are of the order of 2.0–3.0 per cent (Christensen & Hofmann 1994). These estimates exceed the velocity variation our observations imply, and support our view that the source of the heterogeneity is chemical.

CONCLUSIONS

We present evidence for a scattering region beneath Nova Scotia which lies approximately 170 km above the core–mantle boundary. This feature is best described as a scattering region rather than a discontinuity, suggesting that it is a distinct body as opposed to a global layer. An analysis of its properties suggests that it comprises bodies of up to 0.6 to 0.7 km in size within a region of about 690 km^3. The associated *P* velocity perturbation is as high as 0.4 to 0.7 per cent, and *S* perturbation of 1.4 to 6.6 per cent, but its density difference is unconstrained. This evidence rules out partial melting, and suggests that the scattering region is predominantly a result of chemical rather than thermal differences with the surrounding mantle. Such a region may be explained as a remnant of ancient subducted slab, and links small-scale chemical heterogeneity in the lower mantle with subduction. This study therefore provides strong evidence for small-scale chemical heterogeneity in the lower mantle.

ACKNOWLEDGMENTS

LB was supported by a studentship awarded by the British Geological Survey (BGS), funded under AWE contract OCG0385. This paper is published by permission of the Executive Director of the BGS (NERC).

REFERENCES

Boehler, R., 2000. High-pressure experiments and the phase diagram of the lower mantle and core materials, *Rev. Geophys.,* **38,** 221–245.

Chopelas, A. & Boehler, R., 1992. Thermal expansivity in the lower mantle, *Geophys. Res. Lett.,* **19,** 1983–1986.

Christensen, U.R. & Hofmann, A.W., 1994. Segregation of subducted oceanic crust in the convecting mantle, *J. geophys. Res.,* **99,** 19 867–19 884.

Dziewonski, A.M., Chou, T.-A. & Woodhouse, J.H., 1981. Determination of earthquake source parameters from waveform data for studies of global and regional seismicity, *J. geophys. Res.,* **86,** 2825–2852.

Engdahl, E.R., van der Hilst, R. & Buland, R., 1998. Global teleseismic earthquake relocation with improved traveltimes and procedures for depth determination, *Bull. seism. Soc. Am.,* **88,** 722–743.

Engebretson, D.C., Kelley, K.P., Cashman, H.J. & Richards, M.A., 1992. 180 million years of subduction, *GSA Today,* **2,** 93–100.

Freybourger, M., Krüger, F. & Achauer, U., 1999. A 22° long seismic profile for the study of the top of D″, *Geophys. Res. Lett.,* **26,** 3409–3412.

Gaherty, J.B. & Lay, T., 1992. Investigation of laterally heterogeneous shear velocity structure in D″ beneath Eurasia, *J. geophys. Res.,* **97,** 417–435.

Garnero, E.J., Helmberger, D.V. & Engen, G., 1988. Lateral variations near the core-mantle boundary, *Geophys. Res. Lett.,* **15,** 609–612.

Grand, S.P., 1994. Mantle Shear Structure beneath the Americas and Surrounding oceans, *J. Geophys. Res.,* **99,** 11591–11621.

Grand, S.P., van der Hilst, R.D. & Widiyantoro, S., 1997. Global seismic tomography: a snapshot of convection in the Earth, *GSA Today,* **7,** 1–7.

Gutenberg, B., 1913. Über die Konstitution des Erdinnern, erschlossen aus Erdbebenbeobachtungen, *Phys. Z.,* **14,** 1217–1218.

Hedlin, M.A.H., Shearer, P.M. & Earle, P.S., 1997. Seismic evidence for small-scale heterogeneity throughout the Earth's mantle, *Nature,* **387,** 145–150.

Helffrich, G.R. & Wood, B.J., 2001. The Earth's mantle, *Nature,* **412,** 501–507.

Houard, S. & Nataf, H.-C., 1992. Further evidence for the 'Lay discontinuity' beneath northern Siberia and the North Atlantic from short-period *P*-waves recorded in France, *Phys. Earth planet. Inter.,* **72,** 264–275.

Kaneshima, S. & Helffrich, G., 1998. Detection of lower mantle scatterers northeast of the Mariana subduction zone using short-period array data, *J. geophys. Res.,* **103,** 4825–4838.

Kaneshima, S. & Helffrich, G., 1999. Dipping low-velocity layer in the mid-lower mantle: evidence for geochemical heterogeneity, *Science,* **283,** 1888–1891.

Kendall, J.-M. & Helffrich, G., 2001. SPICeD: imaging the deep Earth, *Astron. Geophys.,* **42,** 26–29.

Kendall, J.-M. & Nangini, C., 1996. Lateral variations in D″ below the Caribbean, *Geophys. Res. Lett.,* **23,** 399–402.

Kendall, J.-M. & Shearer, P.M., 1994. Lateral variations in D″ thickness from long-period shear wave data, *J. geophys. Res.,* **99,** 11 575–11 590.

Kennett, B.L.N., Engdahl, E.R. & Buland, R., 1995. Constraints on seismic velocities in the Earth from traveltimes, *Geophys. J. Int.,* **122,** 108–124.

Krüger, F., Weber, M., Scherbaum, F. & Schlittenhardt, J., 1995. Normal and inhomogeneous lowermost mantle and core–mantle boundary under the Arctic and Northern Canada, *Geophys. J. Int.,* **122,** 637–658.

Lay, T. & Helmberger, D.V., 1983. A lower mantle S-wave triplication and the velocity structure of D″, *Geophys. J. R. astr. Soc.,* **75,** 799–837.

Lay, T. & Young, C.J., 1996. Imaging scattering structure in the lower mantle by migration of long-period S waves, *J. geophys. Res.,* **101,** 20 023–20 040.

McFadden, P., Drummond, B. & Kravis, S., 1986. The *N*th-root stack: theory, applications, and examples, *Geophysics,* **51,** 1879–1892.

Muirhead, K., 1968. Eliminating false alarms when detecting seismic events automatically, *Nature,* **217,** 533–534.

Nataf, H.-C. & Houard, S., 1993. Seismic discontinuity at the top of D″: a world-wide feature?, *Geophys. Res. Lett.,* **20,** 2371–2374.

Revenaugh, J. & Jordan, T.H., 1991. Mantle layering from ScS reverberations. 4. The lower mantle and core–mantle boundary, *J. geophys. Res.,* **96,** 19 811–19 824.

Scherbaum, F., Krüger, F. & Weber, M., 1997. Double beam imaging: mapping lower mantle heterogeneities using combinations of source and receiver arrays, *J. geophys. Res.,* **102,** 507–522.

Thomas, C., Weber, M., Wicks, C.W. & Scherbaum, F., 1999. Small scatterers in the lower mantle observed at German broadband arrays, *J. geophys. Res.,* **10,** 15 073–15 088.

van der Hilst, R.D., Widiyantoro, S. & Engdahl, E.R., 1997. Evidence for deep mantle circulation from global tomography, *Nature,* **386,** 578–584.

Vidale, J.E. & Benz, H.M., 1992. Upper-mantle seismic discontinuities and the thermal structure of subduction zones, *Nature,* **356,** 678–683.

Vidale, J.E. & Benz, H.M., 1993. A sharp and flat section of the core–mantle boundary, *Nature,* **359,** 627–629.

Weber, M. & Davis, J.P., 1990. Evidence of a laterally variable lower mantle structure from P- and S-waves, *Geophys. J. Int.,* **102,** 231–255.

Weber, M. & Körnig, M., 1990. Lower mantle inhomogeneities inferred from *PcP* precursors, *Geophys. Res. Lett.,* **17,** 1993–1996.

Weber, M. & Körnig, M., 1992. A search for anomalies in the lowermost mantle using seismic bulletins, *Phys. Earth planet. Inter,* **73,** 1–28.

Weber, M. & Wicks, C.W., Jr, 1996. Reflections from a distant subduction zone, *Geophys. Res. Lett.,* **23,** 1453–1456.

Wu, R.S. & Aki, K., 1985a. Elastic wave scattering by a random medium and the small-scale inhomogeneities in the lithosphere, *J. geophys. Res.,* **90,** 10 261–10 273.

Wu, R.S. & Aki, K., 1985b. Scattering characteristics of elastic waves by an elastic heterogeneity, *Geophysics,* **50,** 582–595.

Wysession, M.E., Lay, T., Revenaugh, J., Williams, Q., Garnero, E.J., Jeanloz, R. & Kellogg, L.H., 1998. The D″ discontinuity and its implications, in *The Core–Mantle Boundary Region*, American Geophysical Union Geodynamics Series 28, pp. 273–297, eds. Gurnis, M., Wysession, M.E., Knittle, E. & Buffett, B.A., American Geophysical Union, Washington, DC.

Young, G.B. & Braile, L.W., 1976. A computer program for the application of Zoeppritz's amplitude equations and Knott's energy equations, *Bull. seism. Soc. Am.,* **66,** 1881–1885.

Zerr, A., Diegeler, A. & Boehler, R., 1998. Solidus of Earth's deep mantle, *Science,* **281,** 243–246.